Chemical Science

ROYAL SOCIETY OF CHEMISTRY

EDGE ARTICLE

View Article Online
View Journal

Cite this: DOI: 10.1039/d5sc06155e

All publication charges for this article have been paid for by the Royal Society of Chemistry

Enhancing long-term morphological stability in BHJ organic solar cells through thermocleavable sidechains under continuous thermal stress

Haoyu Zhao,[a] Jordan Shanahan,[b] Jiyeon Oh,[b] Saroj Upreti,[a] Guorong Ma,[a] Wei You *[b] and Xiaodan Gu *[a]

Received 13th August 2025
Accepted 4th December 2025

DOI: 10.1039/d5sc06155e

rsc.li/chemical-science

Organic solar cells (OSCs) have recently achieved power conversion efficiencies (PCEs) exceeding 20%; however, their long-term operational stability remains a significant barrier to commercialization. A key factor in ensuring sustained device performance is the morphological stability of the bulk heterojunction (BHJ) layer, which is closely linked to the mobilities of the donor and acceptor materials. In this study, we introduce a strategy to enhance morphological and thermal stability by incorporating thermocleavable side chains into both the donor and acceptor components of the active layer. Specifically, we employed a thermocleavable side-chain (TCS) containing conjugated polymer donor, PffBT-4T-TCS, and a similarly functionalized fullerene acceptor, C60-TCS. Upon complete thermal cleavage of the alkyl side chains, the backbone glass transition temperature of PffBT-4T-TCS increased by 60 °C. To assess the morphological stability of the thermocleaved BHJ, we utilized atomic force microscopy coupled with infrared spectroscopy (AFM-IR) to analyze films before and after thermal treatment. Our results demonstrate that the BHJ morphology remains remarkably stable after cleavage, maintaining consistent donor/acceptor composition and surface roughness for over 10 weeks at 85 °C thermal stress conditions. Normalized PCE measurements further confirm that this thermocleavable side-chain strategy offers a promising route to achieve both high efficiency and long-term stability in OSC devices.

Introduction

The performance of organic solar cell (OSC) devices has rapidly advanced since the discovery of low bandgap polymers and fullerene acceptors used as bulk heterojunction layers in the early 2000s.[1,2] The of current state-of-the-art OSC devices have surpassed the 20% benchmark.[3–5] In addition to the impressive progress in device performance, the unique advantages for OSC devices include light weight, flexibility, low cost, and solution processability. However, despite achieving high PCE values, the commercialization of OSC device is hindered by device instabilities.[6–10] External factors, such as oxygen, water, and UV irradiation have been effectively mitigated through encapsulation techniques.[11] However, prolonged exposure to direct sunlight generates heat that strongly impacts the energy collection and conversion process occurring in the BHJ active layer during operation.[12] This often leads to a continuous decline in PCE over time at elevated operating temperatures. The performance degradation is primarily due to morphological changes, as the initially formed BHJ morphology is thermodynamically unstable. During casting, high boiling point additives and/or annealing at elevated temperatures are typically used to optimize the BHJ morphology, aiming to maximize devices' PCEs.[13] However, as the device operating temperatures rise, the regained segmental mobility of the components causes the morphology to evolve spontaneously. This leads to the formation of greater phase separation between the donor and acceptor phases, hindering charge generation and collection, ultimately impairing device performance.[14]

Given the impact of chain dynamics on device performance, inhibiting donor/acceptor chain mobility to raise the barrier against morphological degradation presents an effective strategy for fabricating long-term stable OSC devices under continuous thermal stress.[15] Mobility restriction can be achieved through molecular engineering of the donor and acceptor (*e.g.*, backbone modifications, side-chain engineering, or crosslinking) and/or processing techniques (*e.g.*, annealing to promote the system into more thermal equilibrium state).[12] Backbone rigidity is closely tied to molecular mobility, and increasing the proportion of rigid building blocks in the polymer backbone has been shown to effectively reduce molecular dynamics, for example by raising glass transition temperatures

[a]School of Polymer Science and Engineering, Center for Optoelectronic Materials and Devices, The University of Southern Mississippi, Hattiesburg, MS 39406, USA. E-mail: xiaodan.gu@usm.edu

[b]Department of Chemistry, University of North Carolina at Chapel Hill, Chapel Hill, NC 27599, USA. E-mail: wyou@unc.edu

(T_g).[16–18] Another strategy to enhance active layer stability involves using block copolymers composed of donor and acceptor segments, which can self-assemble into microdomains at thermal equilibrium.[19–22] Additional innovative approach to enhancing device stability is through crosslinking strategies for semiconductive polymers.[23,24] Unfortunately, the performance sacrifices caused by the crosslinked structures make this approach less appealing within the community. In addition to phase separation between donor and acceptor materials, crystallization of either the donor polymer or the small-molecule acceptor can significantly influence device morphology.[25,26] Recent work from our group highlights the cold crystallization behavior of the acceptor Y6; when the temperature exceeds 120 °C, Y6 molecules readily crystallize and phase-separate from PM6, leading to a decline in device performance.[14] It is also worth mentioning that the OSC devices are multi-layered structures, comprising various components, such as electrodes, electron or hole transport layers, and the active layer; failure can occur in any of these layers or at the interfaces between them, which is not a focus here.[6,9–13]

Recently, side-chain engineering with cleavable functional groups has emerged as a promising strategy to enhance device stability. The decomposition of alkyl side chains at elevated temperatures was demonstrated using the P3ET polymer.[27,28] It was observed that the T_g of P3ET increased from 23 to 75 °C after complete side-chain cleavage.[29] Although thermal cleavage effectively raises T_g of the donor above room temperature, thiophene-based donors are not optimized for harvesting red and infrared light, resulting in lower device performance. To achieve both high performance and morphological stability, Shanahan *et al.* synthesized a donor–acceptor (D–A) type thermocleavable donor (PffBT-4T-TCS) and conducted stability measurements. Their results showed that copolymers with 60% thermocleavable content enhanced operational stability, achieving a reasonably high PCE of over >3% under continuous thermal stress at 85 °C.[30] Compared to backbone engineering, side-chain engineering holds similar potential for improving thermal stability due to the abundance of side chains in conjugated polymer systems.

In this work, we advanced the investigation of thermocleavable sidechains on the stability of OSC devices, utilizing both a thermocleavable donor (PffBT-4T-TCS) and a thermocleavable acceptor (C60-TCS) for a more comprehensive study. The reduced chain dynamics of thermocleavable materials, particularly regarding T_g, were thoroughly examined by analyzing trends in T_g enhancement relative to the degree of sidechain cleavage using flash differential scanning calorimetry (Flash DSC). The cleavage efficiency of both the thermocleavable donor and acceptor was evaluated using dynamic and isothermal thermogravimetric analysis (TGA). In addition to thermal analysis, X-ray scattering techniques were employed to study the relationship between film morphology and annealing temperatures. Advanced atomic force microscopy coupled with infrared spectroscopy (AFM-IR) was used to characterize the domain purity and phase behavior in the thermocleavable donor/acceptor blend. Finally, long-term stability under continuous thermal stress was monitored, and the results confirmed that incorporating thermocleavable sidechain effectively enhances operational stability. Our results confirm that thermocleavable conjugated materials are effective candidates for stabilizing morphology under operational thermal stress, due to the significantly reduced molecular mobilities resulted from the removal of alkyl side chains. These findings offer valuable insights for designing the next generation of materials for OSC with both long-term stability and superior performance.

Results

Thermal analysis of thermocleavable side-chain bearing donors and acceptors

We began by examining the cleavage process of the thermocleavable donor polymer, PffBT-4T-TCS, to determine both the onset temperature and the associated efficiency of thermal cleavage. Because the alkyl side chains decompose at elevated temperatures, we performed non-isothermal TGA to correlate the onset of cleavage with the extent of alkyl side-chain decomposition in PffBT-4T-TCS. As noted in our previous study on the cleavage kinetics of thermocleavable thiophene-based P3ET polymers, the heating rate can influence the cleavage onset temperature.[29] Accordingly, we maintained a TGA heating rate of 10 K min^{-1} for this investigation.

The thermocleavable donor polymer PffBT-4T-TCS appeared stable up to 217.5 °C, as shown in Fig. 1a, which is 20 °C higher than that of previously studied thermocleavable donor polymer, P3ET. The rapid weight loss observed thereafter corresponds to the cleavage of alkyl side chains, with a 35% weight loss matching the theoretical fraction of these chains.[30] The next inflection point at 250 °C indicates a second thermal cleavage step (Fig. 1a orange dashed vertical line near the 35% mass loss), in which carboxylic acid groups further dissociate and release carbon dioxide. Since too high a temperature would add too much thermal stress to the donor–acceptor blend and deteriorate the morphology, we limited our annealing temperature to around or slightly lower than the temperature required to cleave the alkyl chain (*vide infra*). Additionally, the thermocleavable acceptor (PCBM derived C60-TCS) was analyzed at a heating rate of 10 K min^{-1}, as shown in Fig. 1e. The onset cleavage temperature for the acceptor was lower, at 189 °C, compared to the donor. The amount of cleaved alkyl side chains for C60-TCS was 11.3%, which matched with theoretical weight of the alkyl sidechains in C60-TCS.

Next, we evaluated the degree of thermocleavage as a function of isothermal annealing temperature to determine whether low-temperature cleavage was a viable option for donor–acceptor thermocleavable conjugated polymers. The degree of thermocleavage, as defined in previous work, represents the extend of alkyl side-chain removal (ω) at various isothermal annealing durations.[29] Isothermal TGA was used to assess cleavage efficiency at annealing temperatures of 140, 200, and 220 °C. Additional isothermal TGA data for both the donor and acceptor at various annealing temperatures are presented in Fig. S1. Fig. 1b shows the cleavage efficiency for PffBT-4T-TCS, where annealing at 140 °C resulted in only 13% of alkyl side chains being cleaved after 10 hours. Similarly, annealing at 200 °C was suboptimal, leaving 20% of the alkyl side chains intact after 10 hours. The

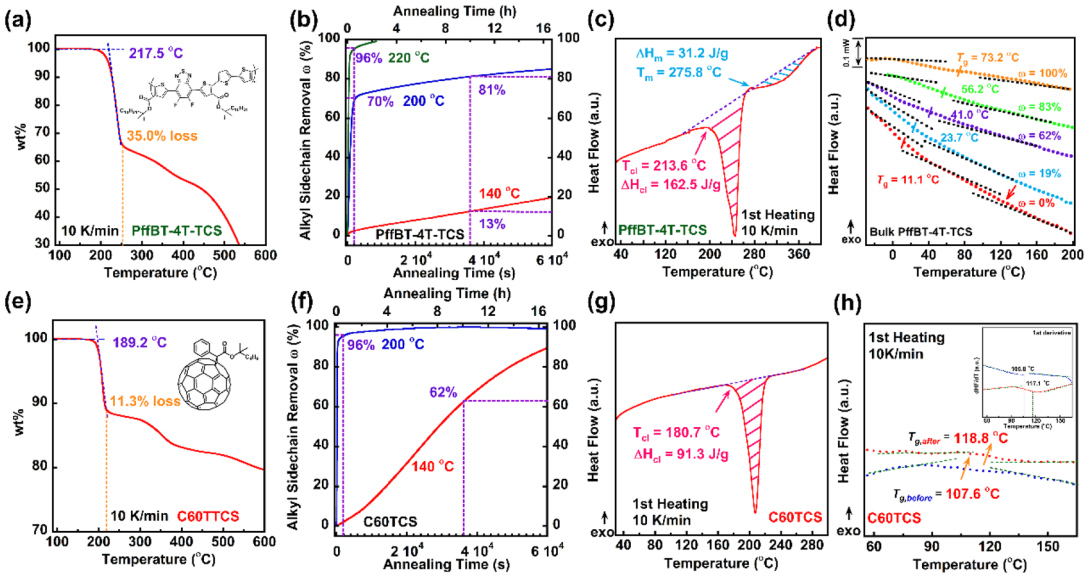

Fig. 1 Thermal analysis of thermocleavable donor and acceptor materials: (a) dynamic TGA of donor PffBT-4T-TCS; (b) cleavage efficiency of PffBT-4T-TCS at 140, 200 and 220 °C under various annealing times; (c) dynamic DSC of the donor showing cleavage enthalpy at a heating rate of 10 K min^{-1}; (d) glass transition temperatures enhancement of the donor at different degrees of cleavage; (e) dynamic TGA of acceptor C60-TCS; (f) cleavage efficiency of C60-TCS at 140 and 200 °C under various annealing times; (g) dynamic DSC of the acceptor showing cleavage enthalpy at a heating rate of 10 K min^{-1}; (h) glass transition temperatures enhancement of the acceptor before and after cleavage.

most effective cleavage occurred at 220 °C, where 96% of alkyl side chains, based on comparison of actual mass loss *vs.* theoretical 100% alkyl sidechain cleavage mass loss, were removed after just 30 minutes of isothermal annealing. For the acceptor C60-TCS, shown in Fig. 1f, 96% of alkyl side chains were cleaved after 30 minutes at 200 °C. Based on the above study of cleavage efficiencies of the donor and acceptor, the final processing condition for the thermocleavable donor/acceptor blend film was set to 220 °C for 30 minutes to balance the thermal stress on the film and the efficiency of cleavage.

A key limitation of previously studied thiophene-based thermocleavable polymer was the absence of any ordered crystalline structure after complete cleavage of the alkyl side chains, due to the melting temperature of P3ET, which is around 160 °C, being lower than the cleavage temperature.[29] One of the innovations of the current thermocleavable donor, PffBT-4T-TCS, is its ability for maintaining crystalline structures even after the alkyl side chains removal. To investigate this, conventional DSC was used to monitor the heat flow of PffBT-4T-TCS samples at a heating rate of 10 K min^{-1}, as shown in Fig. 1c. As the temperature increased, the first endothermic peak reflected the heat absorbed to initiate thermal cleavage, with an onset temperature of 213.6 °C consistent with TGA measurements (Fig. 1a). The red-shaded area represents the total energy required for complete thermal cleavage. By varying isothermal annealing times, the degree of cleavage can be controlled, as noted in previous work.[29] A notable feature of the current D–A thermocleavable donor polymer is the appearance of an additional endothermic peak following the cleavage peak, which can be attributed to the melting of ordered crystalline domains. The melting temperature and enthalpy change associated with this process are indicated by the blue-shaded area (Fig. 1c). In contrast, similar measurements for the uncleaved C60-TCS acceptor, shown in Fig. 1g, revealed no additional endothermic peak beyond the single cleavage peak, indicating that cleaved C60-TCS has an amorphous structure. This matches the observation from the temperature dependent WAXS study, in the following section of the discussion.

Our aim is to improve the morphological stability of the active layer in thermocleavable BHJ blends by increasing the T_g of each component, thereby limiting molecular mobility under continuous thermal stress. The T_g enhancement for PffBT-4T-TCS is shown in Fig. 1d, where heat flow *versus* temperature plots were obtained using flash differential scanning calorimetry (Flash-DSC) due to its superior resolution and sensitivity. As noted earlier, the degree of thermal cleavage can be adjusted by varying the isothermal annealing temperature and duration. The T_g values were determined using the half-step method, and a clear, consistent increase in T_g was observed as the degree of cleavage increased (Fig. 1d). Ultimately, the backbone T_g of fully cleaved PffBT-4T-TCS rose from 11.1 °C in the uncleaved sample to 73.2 °C. Although the thermocleavable acceptor contains only ~11% alkyl side chains, its T_g also increased from 107.6 °C to 118 °C, as illustrated in Fig. 1h. Since the step change was less pronounced for C60-TCS, first derivative plots were included to confirm the validity of the T_g values in Fig. 1h. In summary, thermal analysis confirms that the molecular mobility of both the thermocleavable donor and acceptor can be significantly reduced, as demonstrated by the higher T_g values after side-chain cleavage.

Investigating crystalline structures upon thermal cleavage *via* scattering techniques

As noted earlier, a particularly exciting feature of PffBT-4T-TCS is its potential to better retain or even enhance optoelectronic

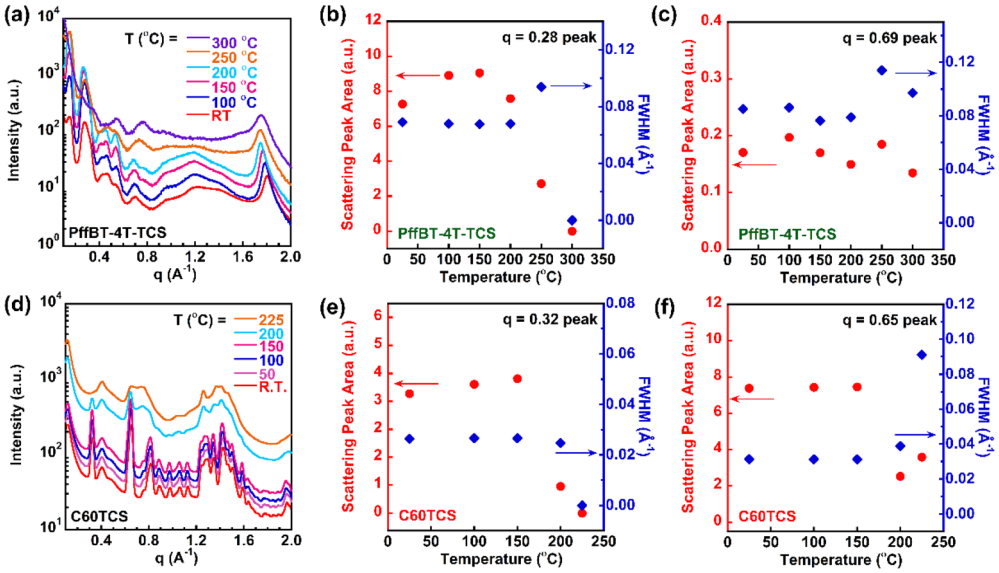

Fig. 2 *In situ* heating WAXS measurement of thermocleavable donor and acceptor: (a) 1D scattering profile of donor at various temperatures; (b) scattering peak area and FWHM for the donor's scattering peak at $q = 0.28$ Å^{-1}; (c) scattering peak area and FWHM for the donor's scattering peak at $q = 0.69$ Å^{-1}; (d) 1D scattering profile of acceptor at various temperatures; (e) scattering peak area and FWHM for the acceptor's peak at $q = 0.32$ Å^{-1}; (f) scattering peak area and FWHM for the acceptor's peak at $q = 0.65$ Å^{-1}.

properties after complete decomposition of alkyl side chains, owing to the persistence of crystalline structures. To investigate this, *in situ* heating WAXS was employed to verify the formation and stability of ordered crystalline domains in the BHJ film during and after thermal cleavage. The corresponding 2D WAXS images were presented in Fig. S2 and S3 for reference.

As shown in Fig. 2a, the donor at room temperature (R. T.) exhibits sharp peaks at $q = 0.28$ Å^{-1} and $q = 1.8$ Å^{-1}, corresponding to alkyl-side chain stacking and π–π stacking, respectively. As the temperature increased from R. T. to 200 °C, the alkyl side-chain peak remained largely unchanged, though a shift in the π–π stacking peak toward a lower q values was observed, due to the thermal expansion of the packing lattice. As cleavage of side-chain began around 220 °C, a significant reduction in peak intensity was observed as the temperature approached 250 °C, as shown by the orange curve in Fig. 2a. At 300 °C, the second stage of the cleavage occurred as noted in the TGA data in Fig. 1a, where the entire side-chains were removed, resulting in the side-chain scattering peak disappeared entirely. The *in situ* heating WAXS measurements allowed us to monitor the cleavage process and the crystalline domain remained as several scattering peaks exist after cleavage, including those at $q = 0.5$ and 0.75 Å^{-1}. To quantitatively track the evolution of key peaks, we plotted changes in peak area and full width at half maximum (FWHM) in Fig. 2b and c, respectively. As shown in Fig. 2b, the peak area and FWHM for alkyl side chains remained stable up to 200 °C, but began to decline at 225 °C and became indistinguishable by 300 °C. Fig. 2c shows that the scattering peak at $q = 0.69$ Å^{-1}, representing the donor's ordered crystalline structure, remained unaffected by the thermal cleavage process, as evidenced by consistent peak area and FWHM values.

We next conducted *in situ* WAXS experiments on the thermocleavable acceptor, C60-TCS, as shown in Fig. 2d. Based on our thermal analysis from DSC and TGA, we hypothesized that the alkyl side chain scattering peak at $q = 0.32$ Å^{-1} would significantly diminish at elevated temperatures. As shown by the light blue curve in Fig. 2d, WAXS data at 200 °C already indicated a notable reduction in the alkyl side-chain scattering peak, which disappeared entirely by 225 °C. Additionally, several scattering peaks in the uncleaved acceptor, ranging from $q = 0.65$ to 1.2 Å^{-1}, either broadened into near amorphous peak or disappeared entirely above 200 °C. Fitted results for the acceptor's scattering peaks at $q = 0.32$ Å^{-1} (alkyl side chains) and $q = 0.65$ Å^{-1} (ordered structures) are presented in Fig. 2e and f, respectively. As shown in Fig. 2e, the alkyl side chain peak area and FWHM for the acceptor, similar to those of the donor, gradually decreased with increasing temperature and were fully eliminated by 225 °C. In contrast to the donor, the acceptor showed no residual ordered structure following complete side-chain cleavage, as indicated by the appearance of a smaller, broader amorphous peak in Fig. 2f. In general, the *in situ* heating WAXS characterizations support our thermal DSC analysis of the thermocleavable donor and acceptor. Both components lost their alkyl side chains upon reaching the cleavage onset temperature, however while the donor retained ordered structures after side-chain cleavage, the acceptor transitioned into an amorphous state. Similar conclusion was reached for 2D GIWAXS for thin film samples, which can be found in Fig. S4.

Phase separation behaviors of BHJ film after thermocleavage and its thermal stability

After benchmarking the cleavage efficiency and evaluating its effects on the T_g and crystalline structure of the individual components, we systematically investigated the morphological behavior of the BHJ active layer composed of thermally cleavable donor and acceptor materials. The morphology of the

PffBT-4T-TCS : C60-TCS (1 : 1.2 ratio) blend film was characterized using AFM-IR, which simultaneously provides surface topography and chemical composition maps. Because AFM-IR relies on distinct absorption peaks for each component in the binary BHJ blend, it was essential to first identify their respective infrared absorption characteristics. To this end, we used Fourier-transform infrared spectroscopy (FTIR) to analyze the absorption peaks of the thermocleavable donor and acceptor before and after cleavage, as shown in Fig. S5. Before cleavage, distinguishable C=O ester stretching peaks were observed at 1709 cm^{-1} and 1736 cm^{-1}, corresponding to ester groups in the donor and acceptor, respectively. After cleavage, the donor's C=O peak at 1709 cm^{-1} split into multiple peaks at 1680, 1690, and 1725 cm^{-1}, while the acceptor's peak at 1736 cm^{-1} shifted to new peaks at 1709, 1725, 1744, and 1755 cm^{-1}. Based on these results, the IR laser for AFM-IR was tuned to 1709 cm^{-1} and 1736 cm^{-1} for the donor and acceptor, respectively, before cleavage, and adjusted to 1680/1690 cm^{-1} and 1744/1755 cm^{-1} after cleavage, depending on the sample's spectral response.

We first examined the as-cast blend film on a silicon wafer to analyze its surface morphology and chemical composition. The AFM height image, IR amplitude overlay, and IR spectral analysis are presented in Fig. 3a–c, respectively. The height image revealed a smooth surface with a root-mean-square-roughness of 1.22 nm. The overlay AFM-IR phase image combines IR amplitude maps obtained at 1709 cm^{-1} and 1736 cm^{-1}. In the overlay image of the as-cast film, excitation at 1709 cm^{-1} corresponds to PffBT-4T-TCS (green areas), while 1736 cm^{-1} corresponds to C60-TCS (red areas). As shown in Fig. 3b, we observed well-mixed regions, where the domain size for donor and acceptor appears comparable. Further nanoscopic spectral analysis in Fig. 3c confirmed the presence of two distinct absorption peaks at 1710 cm^{-1} and 1736 cm^{-1}, consistent with the bulk FTIR spectra and indicative of the donor and acceptor components. Additionally, spectra acquired from positions 1 and 2 (marked with a "+") were nearly identical, further confirming the presence of mixed BHJ domains in the as-cast film.

Thermal treatment (220 °C for 30 minutes) was applied to the as-cast BHJ film, and the post-annealing phase behavior was subsequently assessed using AFM-IR. Following the removal of alkyl side chains, the domain size decreased, while the surface roughness increased to 4.01 nm, suggesting surface coarsening due to thermal cleavage and the formation of shallow depressions (possibly pinholes) from the evaporated alkyl chains, as shown in Fig. 3d. Compared to the as-cast film, the cleaved film's overlay image in Fig. 3e shows smaller domains for both the donor (scanned at 1680 cm^{-1}) and the acceptor (scanned at 1744 cm^{-1}), represented by the green and red commingled regions. The darker regions correspond to lower height areas in Fig. 3d, associated with alkyl side-chain removal from both components. Nanoscopic IR absorption spectra at two locations on the cleaved film revealed that the original peaks for the uncleaved donor (1710 cm^{-1}) and acceptor (1736 cm^{-1}) had fragmented into multiple weaker peaks between 1680 and 1744 cm^{-1}. As established in previous analyses, the local chemical composition correlates with the IR absorption peak area ratio; thus, we used the ratio of the 1709 cm^{-1} to 1725 cm^{-1} peaks reflects the local concentrations of cleaved donor and acceptor.[31] We prepared samples with varying donor-to-acceptor ratios (ranging from 2 : 1 to 1 : 2) and compared the peak area ratios to the theoretical weight percentages, as described in our previous work.[14,31] Peak area calculations were performed by

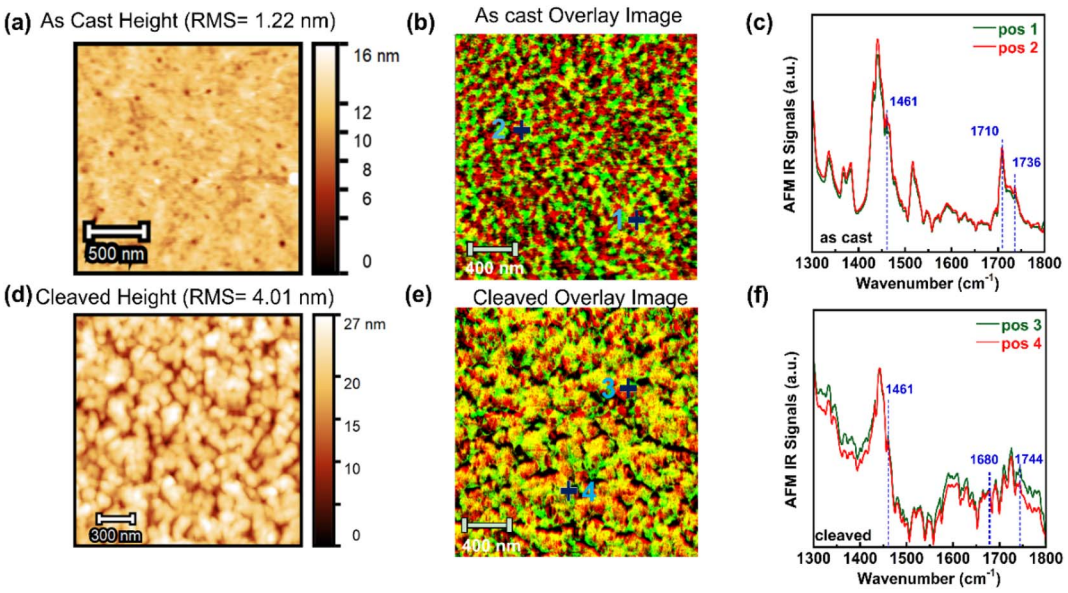

Fig. 3 AFM-IR analysis for PffBT-4T-TCS : C60-TCS (1 : 1.2) blend film morphology: (a) height image of the as-cast blend film, where the RMS surface roughness is noted; (b) overlay image of the as-cast blend film, where green area represents donor contributions and red area represents acceptor contributions; (c) AFM-IR spectra of the as-cast blend film at positions 1 and 2, marked with "+" in the overlay image; (d) height image for the cleaved blend film, where the RMS roughness is noted; (e) overlay image the image of the cleaved blend film, with green area indicating donors and red area representing acceptor contributions; (f) AFM-IR spectra of the cleaved blend film at positions 3 and 4, marked with "+" in the overlay image.

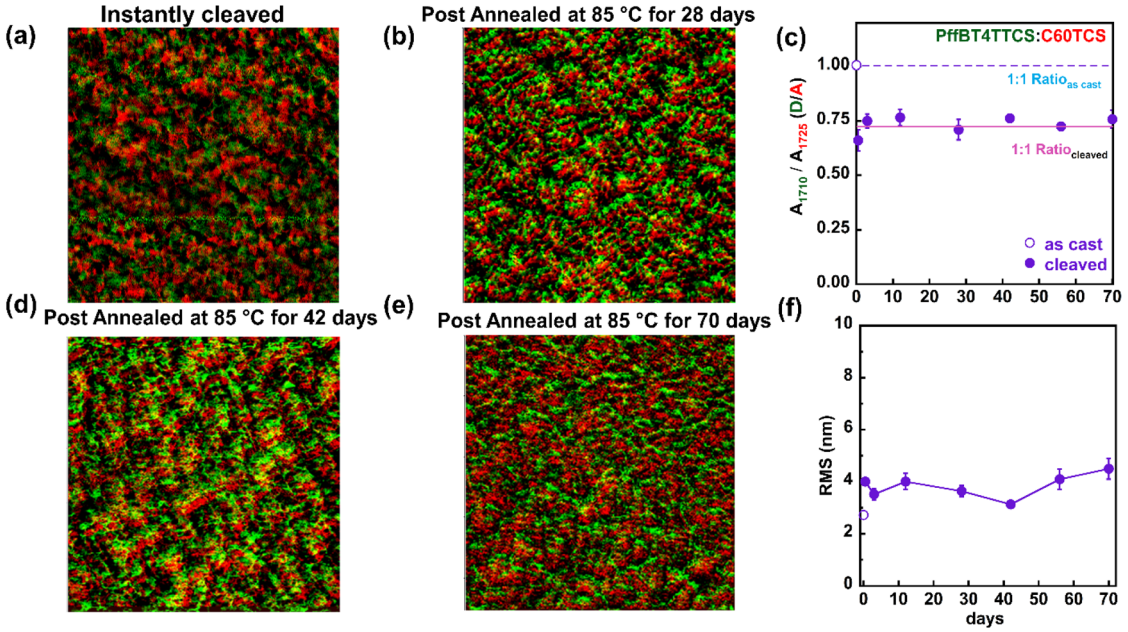

Fig. 4 Stability measurement of the active layer (PffBT-4T-TCS : C60-TCS = 1 : 1) under continuous thermal annealing at 85 °C: (a) overlay image of the cleaved active layer immediately after thermal cleavage; (b) overlay image of the cleaved active layer after annealing at 85 °C for 28 days(c) evolution of local chemical compositions for as-cast and cleaved active layer of a function of annealing time; (d) overlay image of the cleaved active layer after 42 days of annealing at 85 °C; (e) overlay image of the cleaved active layer after 70 days of annealing at 85 °C; (f) surface roughness as a function of annealing time. In all overlay images, green and red regions represent donor and acceptor, respectively.

applying an unbiased baseline and simultaneously fitting the 1709 and 1725 cm^{-1} absorption peaks (Fig. S6). As shown in Fig. S7, the absorption peak area ratio closely matches with the D/A weight percentage, confirming that the 1709/1725 cm^{-1} peak ratio correlates with the local donor–acceptor chemical composition.

A long-term stability test was conducted to evaluate the morphological behavior of the active layer under continuous thermal stress at 85 °C for 10 weeks. The experiment began with a thermally cleaved PffBT-4T-TCS : C60-TCS (1 : 1 wt%) film, and initial surface overlay images were captured, as shown in Fig. 4a. After the initial morphology analysis, the sample was placed on a hot plate inside a glove box and maintained at 85 °C throughout the test duration. Additional representative overlay images were taken after 4, 6, and 10 weeks of continuous thermal annealing, as shown in Fig. 4b, d and e. Domain spacing between donor and acceptor phases was analyzed using circular integration of 2D Fourier transform images. The phase separation size remained nearly constant during the thermal stress period from weeks 4 to 10, at around 100 nm (Fig. S8). Surface roughness (RMS) was also analyzed at various annealing time points, as its fluctuations are linked to morphological stability. As shown in Fig. 4f, the RMS value increased from 2 to 4 nm immediately following cleavage, attributed to surface coarsening. Although the RMS values fluctuated with annealing time, the total variation was limited to 0.5 nm, indicating stable surface morphology throughout the weeks of annealing process. Lastly, we examined the domain purity change using nanoscopic spectroscopy. We investigated four locations on the overlay AFM-IR images for detailed spectral analysis (Fig. S9 and S10). The average 1709/1725 cm^{-1} peak ratio was plotted in Fig. 4c to show the relationship between local donor–acceptor chemical composition ratio and annealing time. The dashed and solid lines represent the theoretical D/A weight ratios for the as-cast and cleaved films, respectively. These results indicate that the local chemical compositions of the as-cast and annealed samples remained stable, closely matching the theoretical values within a margin of error even after 10 weeks of continuous thermal stress.

Device performance and stability of thermocleavable donor/acceptor BHJ

Having successfully established morphological stability of the active layer under continuous thermal stress for over 10 weeks, we proceeded to fabricate a batch of devices incorporating a thermocleavable donor–acceptor BHJ layer, to evaluate long-term device performance stability at an elevated temperature of 100 °C. The devices were constructed in an inverted geometry, with a BHJ layer composed of thermocleavable donor (PffBT-4T-TCS) and thermocleavable acceptor (C60-TCS) in a 1 : 1.2 weight ratio. After thermal treatment to cleave the side-chains and lock in the morphology, the J_{SC} *vs.* V_{OC} curves showed consistent trends and covered area across all samples, indicating stable device performance over extended operational time (Fig. 5a). The device matrix are summarized in Table 1. The device showed consistent PCE over the week long thermal stress, despite the relatively low PCE value around 0.20–0.25% Since the primary focus of this manuscript is to investigate device stability under high temperature after morphology lock-in, we compared the normalized PCE over time for between

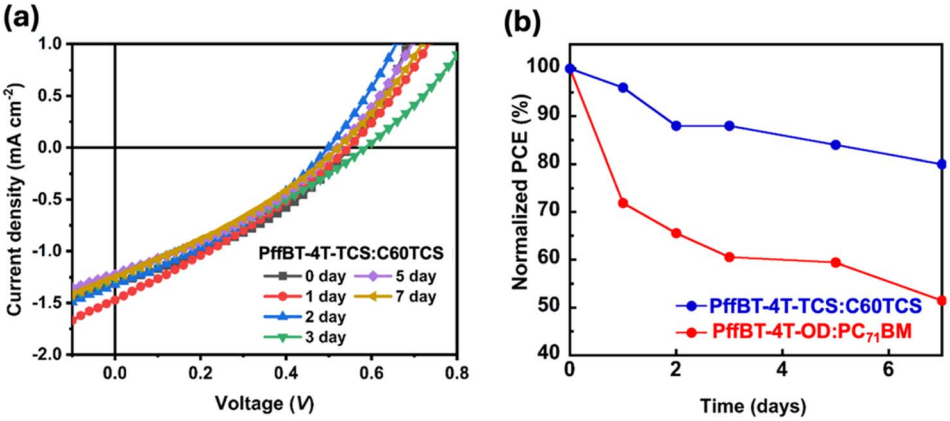

Fig. 5 Device stability test for cleavable materials. (a) Inverted OSC device for 1 : 1.2 thermocleavable donor/acceptor active layer under operational conditions at 100 °C *J*–*V* curves; (b) normalized device performance PCE data for device under continuous thermal stress.

Table 1 Device metrics[a] for BHJ samples outlined in Fig. 5a

Thermal stress duration [day]	V_{oc} [V]	J_{sc} [mA cm^{-2}]	FF [%]	PCE [%]
0	0.260 (0.243 ± 0.01)	2.82 (2.72 ± 0.07)	33.65 (33.53 ± 0.13)	0.25 (0.22 ± 0.02)
1	0.248 (0.236 ± 0.01)	2.51 (2.46 ± 0.04)	33.58 (35.09 ± 0.45)	0.22 (0.20 ± 0.01)
2	0.229 (0.203 ± 0.02)	2.57 (2.57 ± 0.08)	37.66 (36.69 ± 0.48)	0.22 (0.19 ± 0.03)
3	0.218 (0.208 ± 0.01)	2.58 (2.48 ± 0.09)	36.52 (35.70 ± 0.67)	0.21 (0.18 ± 0.01)
5	0.213 (0.183 ± 0.01)	2.57 (2.59 ± 0.07)	37.95 (35.70 ± 0.58)	0.21 (0.17 ± 0.02)
7	0.220 (0.210 ± 0.01)	2.44 (2.42 ± 0.05)	37.93 (37.11 ± 0.56)	0.20 (0.19 ± 0.01)

[a] The statistical values in parentheses are obtained from 10 cells.

devices with thermocleavable and non-thermocleavable active layers. As shown in Fig. 5b, devices incorporating the thermocleavable donor–acceptor blend maintained over 80% of their initial PCE during the testing period, clearly demonstrating their long-term stable stability. On the other hand, the control device PffBT-4T-OD and $PC_{71}BM$ showed a much quicker drop in the normalized PCE, which dropped to around 50% during the 7 days of continuous thermal stress. In other word, although this work did not aim to achieve peak PCE values, the applied thermal treatment effectively stabilized the morphology by cleaving alkyl side chains and raising T_g of the BHJ layer, resulting in OSC devices that retained consistent performance at 100 °C for 7 days. This outcome provided a promising route toward the development of long-term stable and high-performance devices.

Discussions

The T_g is a key indicator of molecular mobility. The difference between the device's operational temperature and the T_g of the active layer blend affects the mobility and behavior of the donor and acceptor phases, given the thermodynamically unstable nature of the mixed D/A phases. Therefore, raising the T_g above the device's operating temperature is a highly effective strategy to enhance the thermal stability of the active layer. In this section, we will discuss various T_g enhancement approaches from the literature and compare them with our current method of using thermal cleavage sidechains.

Backbone engineering is a strategy for increasing polymer's T_g, typically achieved by incorporating rigid building blocks that restrict molecular motion. Our previous work systematically investigated the molecular mobility of PDPPT-series polymers with varying number of thiophene units. We observed that increasing the number of isolated thiophene units from one to three enhanced T_g by over 30 °C, while introducing fused thiophene rings led to T_g increases ranging from 3.5 °C to 22 °C.[32] This concept was also suggested by the Gomez group showing the effective mobility value, can be calculated using an assigned atomic mobility value within each repeat unit to predict T_g.[33] Moreover, we developed a machine learning model capable of quantitatively predicting the dynamic contributions of individual monomer units, thereby enabling the rational design of the next-generation of high T_g donor/acceptor material.[18] A key limitation of both backbone engineering is that, although the backbone T_g can be increased, the T_g of the side-chain region remains low. In dynamic heterogeneous conjugated polymers, where 30–50% of the polymer volume is composed of slow-moving backbones and the remaining side-chains are highly mobile at room temperature. In this case, large-scale rearrangement for polymer chain to allow macro-phase separation is unlikely. However, the local side-chain motion could induce subtle interface rearrangement that compromise device stability.

Our current approach, thermal removal of flexible alkyl side chains, offers a highly effective alternative to above strategies. According to the empirical Fox equation:[34]

$\frac{1}{T_{g,overall}} = \frac{\omega_1}{T_{g,side}} + \frac{\omega_2}{T_{g,back}}$, the overall T_g of a conjugated polymer lies between the T_g values of the side-chain and the backbone. For instance, although the T_g of the polythiophene can exceed 120 °C, the very low T_g of side-chains (∼−70 °C) significantly reduces the overall conjugated polymer's T_g to near room temperature.[35,36] Thus, modifying only the backbone could raise the backbone T_g, but it is rather limited give the high heterogeneity in dynamics for conjugated polymers. Historically, alkyl side-chains has been incorporated into conjugated polymers to improve solubility, enabling solution processing. Therefore, removing side-chains after film deposition is the most effective way to raise T_g, as it eliminates at least 40% of the low T_g components, and yielding T_g increase of over 60 °C, higher than those achieve by other methods. This enhancement can be realized *via* brief thermal treatment, with the cleavage process tunable by temperature and duration. While thermal cleavage effective raises T_g, the loss of cleaved side chains can also affect film morphology. Thus, a careful balance must be struck between maximizing thermal stability and preserving device performance.

On the other hand, a control study is valuable for understating how thermally cleavable sidechains influence OSC performance under operational conditions. Our original motivation to introduce cleavable side chains to PCE11 (the non-cleavable analogue which achieved over 10% PCE with PCBM) was driven by stability investigations of this BHJ system, particularly its morphological instability.[37] In that study, Brebec and co-workers reported that the PCBM domains grow in size under operational conditions, as the acceptor molecules diffuse out of the finely mixed donor–acceptor regions, leading to morphological instability and the formation of larger fullerene aggregates in the aged BHJ layer.[37]

In addition to morphological studies, the device performances of non-cleavable counterparts were previously compared from our recent work[30] focusing on influences of conventional acceptor PCBM. Moreover, we have also identified other reports demonstrating that non-cleavable devices exhibit rapid PCE degradation under thermal stress. For instance, Durrant and co-workers investigated the stability of PffBT4T-2OD:$PC_{71}BM$ and EH-IDTBR systems[38] and found that the normalized PCE of PffBT4T-2OD:$PC_{71}BM$ dropped to 35% after only 50 hours of aging, whereas our device retained 80% of its initial PCE even after months of thermal exposure. They attributed this degradation to a ∼50% increase in charge-carrier density at 85 °C, which led to a higher density of electronic trap states. Another literature[39] also illustrated if the morphology is not "locked", the normalized PCE would significantly reduce in short time period at elevated temperature conditions. In this case, the binary blends dropped 50% PCE over the period of 1 hour.

Conclusion

The use of thermocleavable donors and acceptors has proven to be one of the most effective approaches to increase the T_g of active layer components, thereby suppressing molecular mobility and enabling stable morphology under continuous thermal stress. In this study, we demonstrated that a novel donor–acceptor-type conjugated polymer donor with thermocleavable alkyl side chains can achieve a T_g increase of over 60 °C through thermal annealing at 220 °C for 30 minutes. Additionally, we report for the first time that a fullerene-based acceptor bearing thermocleavable side chains successfully undergoes side-chain removal at a lower temperature, further contributing to thermal stability of the BHJ blend. The BHJ active layer composed of both thermocleavable donor and acceptor exhibited excellent morphological stability over a 10-week period under continuous annealing at 85 °C. This stability was evidenced by consistent local chemical composition, minimal surface roughness variation, and preserved donor–acceptor domain spacing. Furthermore, OSC devices incorporating the side-chain cleaved BHJ layer retained over 80% of their initial PCE after one week of operation at 100 °C, confirming their exceptional thermal durability. Future research should focus on optimizing the balance between morphological stability and device performance in thermocleavable systems. This strategy holds great promise for enabling the next generation of OSCs that combine high energy conversion efficiency with long-term operational stability.

Experimental section

Materials

2-Bromo-2-phenylacetic acid was purchased from Ambeed, Inc. and fullerene was purchased from Sigma Aldrich and were used without further purification.

Synthesis of materials

(1). 2-Bromo-2-phenylacetic acid (6.665 g, 1 eq., 31.000 mmol) and oxalyl dichloride (4.3280 g, 2.92 mL, 1.1 eq., 34.100 mmol) was added to a 100 mL round bottom flask with DCM (25 mL). *N*,*N*-Dimethylformamide (453.2 mg, 480 μL, 0.2 eq., 6.2000 mmol) was then added to the open flask and left stirring for 2 h to form acyl chloride. The solution was then concentrated under reduced pressure to remove excess oxalyl dichloride. To a separate 50 mL 2-neck round bottom flask with reflux condenser, pyridine (2.452 g, 2.50 mL, 1 eq., 31.000 mmol) and 2-methylhexan-2-ol (7.2044 g, 2.00 eq., 62.000 mmol) was dissolved in DCM (25 mL). The acyl chloride was redissolved in 5 mL of DCM and added dropwise the alcohol solution at room temperature, then heated to 40 °C for 18 hours. The solution was then added to 500 mL of water and extracted with ethyl acetate 3×, washed with brine and dried over $MgSO_4$. The crude product was further purified by column chromatography 1 : 1 DCM : hexane to yield 2-methylhexan-2-yl 2-bromo-2-phenylacetate (5.421 g, 17.31 mmol, 55.83%). ^{1}H NMR (400 MHz, $CDCl_3$) δ 7.58–7.43 (m, 2H), 7.40–7.30 (m, 3H), 5.24 (s, 1H), 1.70 (m, 2H), 1.42 (s, 6H), 1.29–1.01 (m, 4H), 0.83 (t, J = 7.2 Hz, 3H) (Scheme 1).

C60-TCS. Fullerene (1000 mg, 1 eq., 1.388 mmol) and 2-methylhexan-2-yl 2-bromo-2-phenylacetate (652.0 mg, 1.5 eq., 2.081 mmol) was dissolved in toluene (120 mL) in a 500 mL

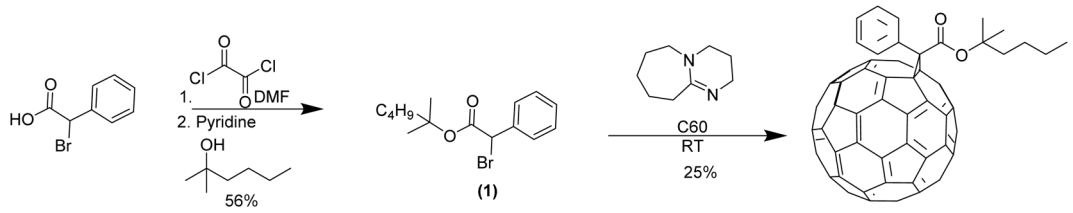

Scheme 1 Synthesis of C60-TCS.

round bottom flask. After most material was dissolved 2,3,4,6,7,8,9,10-octahydropyrimido[1,2-*a*]azepine (316.9 mg, 311 μL, 1.5 eq., 2.081 mmol) was added to the solution. The reaction was left stirring at room temperature for 18 h. Silica gel was next added to the solution and solvent was evaporated. The product was then purified by column chromatography. Hexane to wash away fullerene followed by 1 : 1 toluene : hexane. The product fractions were concentrated again and precipitated in acetone and washed through centrifugation three times. Excess solvent was evaporated by high vacuum to give [6,6] phenyl-C61-acetic acid-2,2-methyl-hexyl ester, C60-TCS (325 mg, 341 μmol, 24.6%). ^{1}H NMR (600 MHz, $CDCl_3$) δ 8.16–8.04 (m, 2H), 7.60–7.47 (m, 3H), 1.87–1.78 (m, 2H), 1.30–1.15 (m, 6H), 0.84 (t, J = 7.1 Hz, 3H). ^{13}C NMR (151 MHz, $CDCl_3$) δ 165.40, 147.76, 146.49, 145.47, 145.26, 145.11, 145.10, 145.08, 145.03, 144.73, 144.65, 144.60, 144.59, 144.50, 144.33, 144.23, 143.83, 143.64, 143.04, 142.96, 142.91, 142.89, 142.86, 142.83, 142.32, 142.13, 142.07, 140.91, 140.86, 138.08, 137.67, 133.00, 132.08, 129.07, 128.49, 86.29, 76.11, 57.32, 40.43, 25.99, 25.90, 22.90, 14.05. The related synthetic route is listed below, and the corresponding NMR results were shown in SI from Fig. S11–S13.

Characterization techniques

DSC. A Mettler-Toledo DSC (DSC 3+) was used to monitor the thermal cleavage process with an indium standard was used to calibrate the heat flow and onset of melting at 10 K min^{-1} heating rate. A Mettler-Toledo Flash differential scanning calorimeter (Flash DSC 2+) was used for T_g measurement of thermocleavable donor and acceptor materials. The ultra-fast standard chip capable of heating and cooling rates up to 4000 K s^{-1} was employed in Flash DSC. All measurements were conducted under nitrogen flow (60 mL min^{-1}) at ambient pressure.

TGA. Thermal gravimetric analysis (TGA) was performed using a Mettler-Toledo TGA/DSC 3+ thermogravimetric analyzer under a nitrogen atmosphere. Dynamic heating was conducted from 25 to 600 °C and isothermal heating was maintained for 24 hours.

WAXS. WAXS of sample powder was performed using a laboratory beamline system (Xenocs Inc. Xeuss 2.0) with an X-ray wavelength of 1.54 Å and a sample-to-detector distance of 15 cm. Samples were maintained under vacuum to minimize air scattering and temperature was controlled using a thermal stage (Linkam HFSX350-GI). Scattering images were recorded on a Pilatus 1M detector (Dectris Inc.) with an exposure time of 15 minutes for transmission mode and 2 hours for grazing incidence mode. For grazing incidence mode, samples were exposed at a fixed incidence angle of 0.2°. Data were processed using the Nika package and WAXSTools packages in Igor Pro (Wavemetrics).

AFM-IR. AFM-IR was performed using NanoIR3 system (Anasys Instrument Inc) coupled with a MIRcat-QT™ quantum cascade mid-infrared laser (frequency range of 917–1700 cm^{-1} and repetition rate of 1470 kHz). AFM-IR measurements were collected in tapping mode using a gold-coated AFM probe (spring constant of 40 N m^{-1} and resonant frequency of 300 kHz). The pulsed mid-IR laser was tuned to absorption bands characteristic of each component, as determined by FTIR (1709 cm^{-1} for uncleaved PffBT-4T-TCS and 1736 cm^{-1} for uncleaved C60-TCS). Acquired images were flattened using Anasis Studio software.

Device characterizations. Devices were fabricated with the following layer structure: ITO/ZnO/PffBT-4T-TCS donor:C60-TCS acceptor/MoO_3/Al, where ITO, ZnO, and MoO_3 refer to indium tin oxide, zinc oxide, and molybdenum oxide, respectively. Patterned ITO-coated glass substrates (size of 1.5 cm × 1.5 cm) were cleaned sequentially with detergent, acetone, and isopropanol for 15 minutes. The substrates were then treated with ultraviolet-ozone plasma for 15 min. A ZnO solution was spin-coated at 3500 rpm 60 seconds onto the ITO surface, followed by annealing at 200 °C for 1 hour in air. The ZnO-coated substrates were then transferred into a nitrogen filled glovebox. The solutions of the active layer were prepared with a donor : acceptor ratio of 1 : 1.2 in a mixed solvent of CB : o-DCB (50 : 50 volume ratio). For PffBT-4T-TCS:C60-TCS solution, the concentration was 40 mg mL^{-1}. All solutions were stirred at 150 °C for 2 hours before spin coating. Note that all substrates were preheated on a hot plate at 120 °C. The solutions were spin-coated onto the ZnO layer to form a ∼200 nm-thick films. Next, the BHJ films were thermally annealed at 220 °C for 30 minutes to induce thermal cleavage of the sidechains. Finally, MoO_3 (thickness: 10 nm) and Al (thickness: 100 nm) were deposited under vacuum (<5.0 × 10^{-6} Pa). The active area of each device was 0.068 cm^2.

Author contributions

X. G. and W. Y. conceived and supervised the project. H. Z. performed the thermal and microscopy analyses. J. S. synthesized the donor and acceptor materials. J. O. carried out device fabrication. G. M. performed the X-ray analysis. H. Z. drafted the initial manuscript, and all authors contributed to reviewing and revising the work.

Conflicts of interest

There are no conflicts to declare.

Data availability

The data that support the findings of this study are available from the corresponding authors upon reasonable request.

Supplementary information: further details of thermal analysis, microscopy, NMR, and X-ray characterization. See DOI: https://doi.org/10.1039/d5sc06155e.

Acknowledgements

H. Z. and X. G. thanks the Office of Naval Research (ONR) for supporting various thermal and morphology characterization under contract number of N00014-23-1-2063. J. S., J. O., and W. Y. acknowledges the support from the National Science Foundation (NSF) under award DMR-2210586 to enable the synthesis of materials used in this study and device characterization.

References

1 G. Zhang, F. R. Lin, F. Qi, T. Heumüller, A. Distler, H.-J. Egelhaaf, N. Li, P. C. Y. Chow, C. J. Brabec, A. K. Y. Jen, *et al.*, Renewed Prospects for Organic Photovoltaics, *Chem. Rev.*, 2022, **122**(18), 14180–14274, DOI: 10.1021/acs.chemrev.1c00955.

2 Y. Liu, B. Liu, C.-Q. Ma, F. Huang, G. Feng, H. Chen, J. Hou, L. Yan, Q. Wei, Q. Luo, *et al.*, Recent progress in organic solar cells (Part I material science), *Sci. China:Chem.*, 2022, **65**(2), 224–268, DOI: 10.1007/s11426-021-1180-6.

3 L. Zhu, M. Zhang, G. Zhou, Z. Wang, W. Zhong, J. Zhuang, Z. Zhou, X. Gao, L. Kan, B. Hao, *et al.*, Achieving 20.8% organic solar cells *via* additive-assisted layer-by-layer fabrication with bulk p-i-nstructure and improved optical management, *Joule*, 2024, **8**(11), 3153–3168, DOI: 10.1016/j.joule.2024.08.001.

4 Y. Jiang, S. Sun, R. Xu, F. Liu, X. Miao, G. Ran, K. Liu, Y. Yi, W. Zhang and X. Zhu, Non-fullerene acceptor with asymmetric structure and phenyl-substituted alkyl side chain for 20.2% efficiency organic solar cells, *Nat. Energy*, 2024, **9**(8), 975–986, DOI: 10.1038/s41560-024-01557-z.

5 R. Ma, Z. Luo, Y. Zhang, L. Zhan, T. Jia, P. Cheng, C. Yan, Q. Fan, S. Liu, L. Ye, *et al.*, Organic solar cells: beyond 20%, *Sci. China Mater.*, 2025, **68**(6), 1689–1701, DOI: 10.1007/s40843-025-3366-9.

6 C. Müller, On the Glass Transition of Polymer Semiconductors and Its Impact on Polymer Solar Cell Stability, *Chem. Mater.*, 2015, **27**(8), 2740–2754, DOI: 10.1021/acs.chemmater.5b00024.

7 Q. Burlingame, M. Ball and Y.-L. Loo, It's time to focus on organic solar cell stability, *Nat. Energy*, 2020, **5**(12), 947–949, DOI: 10.1038/s41560-020-00732-2.

8 Y. Wang, J. Lee, X. Hou, C. Labanti, J. Yan, E. Mazzolini, A. Parhar, J. Nelson, J.-S. Kim and Z. Li, Recent Progress and Challenges toward Highly Stable Nonfullerene Acceptor-Based Organic Solar Cells, *Adv. Energy Mater.*, 2021, **11**(5), 2003002, DOI: 10.1002/aenm.202003002.

9 P. Ding, D. Yang, S. Yang and Z. Ge, Stability of organic solar cells: toward commercial applications, *Chem. Soc. Rev.*, 2024, **53**(5), 2350–2387, DOI: 10.1039/D3CS00492A.

10 J. Yu, S. Li, M. Shi, H. Zhu and H. Chen, Recent Advances in Thermo- and Photostabilities of Organic Solar Cells: Material Design and Morphology Control, *Polym. Sci. Technol.*, 2025, **1**(1), 25–45, DOI: 10.1021/polymscitech.4c00054.

11 X. Xu, D. Li, J. Yuan, Y. Zhou and Y. Zou, Recent advances in stability of organic solar cells, *EnergyChem*, 2021, **3**(1), 100046, DOI: 10.1016/j.enchem.2020.100046.

12 P. Cheng and X. Zhan, Stability of organic solar cells: challenges and strategies, *Chem. Soc. Rev.*, 2016, **45**(9), 2544–2582, DOI: 10.1039/C5CS00593K.

13 M. Ghasemi, N. Balar, Z. Peng, H. Hu, Y. Qin, T. Kim, J. J. Rech, M. Bidwell, W. Mask, I. McCulloch, *et al.*, A molecular interaction–diffusion framework for predicting organic solar cell stability, *Nat. Mater.*, 2021, **20**(4), 525–532, DOI: 10.1038/s41563-020-00872-6.

14 H. Zhao, N. Prine, S. Kundu, G. Ma and X. Gu, Effect of Thermal Stress on Morphology in High-Performance Organic Photovoltaic Blends, *JACS Au*, 2024, **4**(11), 4334–4344, DOI: 10.1021/jacsau.4c00631.

15 Z. Cao, Z. Li, A. Awada, S. A. Tolba, M. Mooney, Y. Wang, Y.-C. Chiu, S. Rondeau-Gagné, W. Xia and X. Gu, Approaching highly stable optoelectronic device operation at elevated temperature by locking backbone torsion of conjugated polymers, *Matter*, 2025, 102195, DOI: 10.1016/j.matt.2025.102195.

16 Z. Qian, Z. Cao, L. Galuska, S. Zhang, J. Xu and X. Gu, Glass Transition Phenomenon for Conjugated Polymers, *Macromol. Chem. Phys.*, 2019, **220**(11), 1900062, DOI: 10.1002/macp.201900062.

17 S. Zhang, A. Alesadi, M. Selivanova, Z. Cao, Z. Qian, S. Luo, L. Galuska, C. Teh, M. U. Ocheje, G. T. Mason, *et al.*, Toward the Prediction and Control of Glass Transition Temperature for Donor–Acceptor Polymers, *Adv. Funct. Mater.*, 2020, **30**(27), 2002221, DOI: 10.1002/adfm.202002221.

18 A. Alesadi, Z. Cao, Z. Li, S. Zhang, H. Zhao, X. Gu and W. Xia, Machine learning prediction of glass transition temperature of conjugated polymers from chemical structure, *Cell Rep. Phys. Sci.*, 2022, **3**(6), 100911, DOI: 10.1016/j.xcrp.2022.100911.

19 Y. Lee and E. D. Gomez, Challenges and Opportunities in the Development of Conjugated Block Copolymers for Photovoltaics, *Macromolecules*, 2015, **48**(20), 7385–7395, DOI: 10.1021/acs.macromol.5b00112.

20 C. Guo, Y.-H. Lin, M. D. Witman, K. A. Smith, C. Wang, A. Hexemer, J. Strzalka, E. D. Gomez and R. Verduzco, Conjugated Block Copolymer Photovoltaics with near 3% Efficiency through Microphase Separation, *Nano Lett.*, 2013, **13**(6), 2957–2963, DOI: 10.1021/nl401420s.

21 Z. Guo, A. Plant, J. Del Mundo, J. H. Litofsky, B. Liu, R. J. L. Hallman, E. W. Gomez, M. A. Hickner, Y. Lee and E. D. Gomez, Fully conjugated block copolymers enhance thermal stability of polymer blend solar cells, *Polymer*, 2023, **288**, 126465, DOI: 10.1016/j.polymer.2023.126465.

22 Y.-H. Lee, W.-C. Chen, C.-J. Chiang, K.-C. Kau, W.-S. Liou, Y.-P. Lee, L. Wang and C.-A. Dai, A new strategy for

fabricating organic photovoltaic devices with stable D/A double-channel network to enhance performance using self-assembling all-conjugated diblock copolymer, *Nano Energy*, 2015, **13**, 103–116, DOI: 10.1016/j.nanoen.2015.01.022.

23 G. Wantz, L. Derue, O. Dautel, A. Rivaton, P. Hudhomme and C. Dagron-Lartigau, Stabilizing polymer-based bulk heterojunction solar cells *via* crosslinking, *Polym. Int.*, 2014, **63**(8), 1346–1361, DOI: 10.1002/pi.4712.

24 F.-J. Kahle, C. Saller, A. Köhler and P. Strohriegl, Crosslinked Semiconductor Polymers for Photovoltaic Applications, *Adv. Energy Mater.*, 2017, **7**(16), 1700306, DOI: 10.1002/aenm.201700306.

25 Q. Liang, M. Duan, X. Liu, H. Zhu, K. Yang, W. Zhang, J. Xin and J. Liu, Recent advances in effect of crystallization dynamics process on the morphology of active layer in organic solar cells, *Battery Energy*, 2024, **3**(4), 20230073, DOI: 10.1002/bte2.20230073.

26 W. Zhu, A. P. Spencer, S. Mukherjee, J. M. Alzola, V. K. Sangwan, S. H. Amsterdam, S. M. Swick, L. O. Jones, M. C. Heiber, A. A. Herzing, *et al.*, Crystallography, Morphology, Electronic Structure, and Transport in Non-Fullerene/Non-Indacenodithienothiophene Polymer:Y6 Solar Cells, *J. Am. Chem. Soc.*, 2020, **142**(34), 14532–14547, DOI: 10.1021/jacs.0c05560.

27 J. F. Ponder Jr, S. A. Gregory, A. Atassi, A. K. Menon, A. W. Lang, L. R. Savagian, J. R. Reynolds and S. K. Yee, Significant Enhancement of the Electrical Conductivity of Conjugated Polymers by Post-Processing Side Chain Removal, *J. Am. Chem. Soc.*, 2022, **144**(3), 1351–1360, DOI: 10.1021/jacs.1c11558.

28 S. Y. Son, S. Samson, S. Siddika, B. T. O'Connor and W. You, Thermocleavage of Partial Side Chains in Polythiophenes Offers Appreciable Photovoltaic Efficiency and Significant Morphological Stability, *Chem. Mater.*, 2021, **33**(12), 4745–4756, DOI: 10.1021/acs.chemmater.1c01305.

29 H. Zhao, J. J. Shanahan, S. Samson, Z. Li, G. Ma, N. Prine, L. Galuska, Y. Wang, W. Xia, W. You, *et al.*, Manipulating Conjugated Polymer Backbone Dynamics through Controlled Thermal Cleavage of Alkyl Side Chains, *Macromol. Rapid Commun.*, 2022, **43**(24), 2200533, DOI: 10.1002/marc.202200533.

30 J. Shanahan, J. Oh, S. Y. Son, S. Siddika, D. Pendleton, B. T. O'Connor and W. You, Strategic Incorporation of Cleavable Side Chains Improves Thermal Stability of PffBT-T4-Based Polymer Solar Cells, *Chem. Mater.*, 2023, **35**(23), 10139–10149, DOI: 10.1021/acs.chemmater.3c02181.

31 N. Prine, Z. Cao, S. Zhang, T. Li, C. Do, K. Hong, C. Cardinal, T. L. Thornell, S. E. Morgan and X. Gu, Enabling quantitative analysis of complex polymer blends by infrared nanospectroscopy and isotopic deuteration, *Nanoscale*, 2023, **15**(16), 7365–7373, DOI: 10.1039/D3NR00886J.

32 S. Zhang, M. U. Ocheje, L. Huang, L. Galuska, Z. Cao, S. Luo, Y.-H. Cheng, D. Ehlenberg, R. B. Goodman, D. Zhou, *et al.*, The Critical Role of Electron-Donating Thiophene Groups on the Mechanical and Thermal Properties of Donor–Acceptor Semiconducting Polymers, *Adv. Electron. Mater.*, 2019, **5**(5), 1800899, DOI: 10.1002/aelm.201800899.

33 R. Xie, A. R. Weisen, Y. Lee, M. A. Aplan, A. M. Fenton, A. E. Masucci, F. Kempe, M. Sommer, C. W. Pester, R. H. Colby, *et al.*, Glass transition temperature from the chemical structure of conjugated polymers, *Nat. Commun.*, 2020, **11**(1), 893, DOI: 10.1038/s41467-020-14656-8.

34 T. G. Fox, Influence of diluent and of copolymer composition on the glass temperature of a polymer system, *Bull. Am. Phys. Soc.*, 1952, **1**, 123.

35 S. A. Chen and J. M. Ni, Structure/properties of conjugated conductive polymers. 1. Neutral poly(3-alkythiophene)s, *Macromolecules*, 1992, **25**(23), 6081–6089, DOI: 10.1021/ma00049a001.

36 R. Xie, Y. Lee, M. P. Aplan, N. J. Caggiano, C. Müller, R. H. Colby and E. D. Gomez, Glass Transition Temperature of Conjugated Polymers by Oscillatory Shear Rheometry, *Macromolecules*, 2017, **50**(13), 5146–5154, DOI: 10.1021/acs.macromol.7b00712.

37 N. Li, J. D. Perea, T. Kassar, M. Richter, T. Heumueller, G. J. Matt, Y. Hou, N. S. Güldal, H. Chen, S. Chen, *et al.*, Abnormal strong burn-in degradation of highly efficient polymer solar cells caused by spinodal donor-acceptor demixing, *Nat. Commun.*, 2017, **8**, 14541.

38 H. Cha, J. Wu, A. Wadsworth, J. Nagitta, S. Limbu, S. Pont, Z. Li, J. Searle, M. F. Wyatt, D. Baran, *et al.*, An Efficient, "Burn in" Free Organic Solar Cell Employing a Nonfullerene Electron Acceptor, *Adv. Mater.*, 2017, **29**(33), 1701156, DOI: 10.1002/adma.201701156.

39 P. Cheng, C. Yan, T.-K. Lau, J. Mai, X. Lu and X. Zhan, Molecular Lock: A Versatile Key to Enhance Efficiency and Stability of Organic Solar Cells, *Adv. Mater.*, 2016, **28**(28), 5822–5829, DOI: 10.1002/adma.201600426.